Spatiotemporal lipid profiling during early embryo development of *Xenopus laevis* using dynamic Time-of-Flight Secondary Ion Mass Spectrometry (ToF-SIMS) Imaging

Hua Tian(田华)*[†], John S. Fletcher*[§], Raphael Thuret[§], Alex Henderson*, Nancy Papalopulu[§], John C. Vickerman* and Nicholas P. Lockyer[‡]

The paper is submitted from the University of Manchester.

Abbreviated title: Lipids profiling of *Xenopus laevis* embryo using ToF-SIMS imaging

Manchester Institute of Biotechnology, School of Chemical Engineering and Analytical Science*, Faculty of Life Science[§] and Manchester Institute of Biotechnology, School of Chemistry[‡], The University of Manchester, UK

[†]Present address: Department of Chemistry, Pennsylvania State University, US; [§]Present Address: Department of Chemistry and Molecular Biology, University of Gothenburg, Sweden.

Correspondence,

Nicholas P. Lockyer

Tel: +44 (0)161 306 4479

E-mail: Nick.Lockyer@manchester.ac.uk

Abstract

Time-of-Flight secondary ion mass spectrometry (ToF-SIMS) imaging has been used for the direct analysis of single intact *Xenopus laevis* (*X. laevis*) embryo surfaces, locating multiple lipids during fertilisation and the early embryo development stages with sub-cellular lateral resolution (~4 µm). The method avoids the complicated sample preparation for lipid analysis of the embryos, which requires selective chemical extraction of a pool of samples and chromatographic separation, while preserving the spatial distribution of biological species. The results show ToF-SIMS is capable of profiling multiple components (*e.g.*, glycerophosphocholine, sphingomyelin, cholesterol, vitamin E, diacylglycerol, triacylglycerol) in a single *X. laevis* embryo. We observe lipid remodelling during fertilisation and early embryo development *via* time course sampling. The study also reveals the lipid distribution on the gametes fusion site. The methodology used in the study opens the possibility of studying developmental biology using high resolution imaging MS and of understanding the functional role of the biological molecules.

Key words: Oocyte · embryo · *Xenopus laevis* · Time-of-flight secondary ion mass spectrometry · lipid profiling · Mass spectrometry imaging

Introduction

The location and identification of lipids is essential to understand their role in biological processes. Their distribution in a cell membrane, nucleus, or other organelles is responsible for their function in inter- and intra-cellular communication and signalling (1, 2). To date, lipid profiling of *Xenopus laevis* (*X. laevis*) embryos has been accomplished using a selective organic extraction methodology followed by gas/liquid chromatographic separation coupled with mass spectrometry (GC-MS/LC-MS). Comprehensive work on the membrane composition of the *X. laevis* oocyte has been reported by Hill and co-workers (3). Lipid species in the mass range *m/z* 400-950 were detected. The plasma membrane is rich in glycerophosphocholine (GPCho), sphingomyelin (SM) and glycerophosphoinositol (GPIns) as well as cholesterol comprising approximately 20% of the total lipid extraction. Huang *et al.* (4) examined the fatty acid composition of egg yolk in three anuran species. Koek *et al.* (5) analysed approximately 10% of the cytoplasm in a single *X. laevis* oocyte using GC/MS. The detected compounds include organic acids, fatty acids (saturated, unsaturated, and hydroxy fatty acids ranging from C8 to C28), amino acids, alcohols, and sugars. These techniques, based on solvent extraction, do not provide any information on spatial localisation beyond the fraction which was extracted, however, they offer qualitative and quantitative information about the composition of the cytoplasm with respect to key lipid compounds (6).

A current challenge in lipid biology studies is determining the spatial location of multiple lipids while retaining compositional information. Techniques such as scanning electron microscopy (SEM) and confocal microscopy have been applied to image the frog egg and embryo to investigate the mechanisms of biological processes and embryo development. Monroy *et al.* (7) first revealed the outer surface of the plasma membrane in *X. laevis* egg by means of SEM. The architecture of the membrane exhibits dramatic changes before and after fertilisation and as the fertilised egg moves towards the two-cell embryo. The large hemispherical protrusions on the

unfertilised egg gradually become smooth and the microvilli withdraw along with completion of the fertilisation and first cleavage. However, these previous studies were either focused on lipid component identification or on surface morphology after complicated sample preparation protocols. Immunofluorescence has revealed cortical and subcortical actin filaments and surface microvilli in late stage and highlighted certain organelles within *X. laevis* oocytes (8, 9), but this method has been questioned because of the possible interference of the fluorescent tags on *in-vivo* function (10-12).

Mass spectrometric imaging (MSI) is capable of detecting lipid species in intact biological cells and tissue, and providing lateral resolution down to the micron scale (13-15). Ferreira et al. (16) used matrix-assisted laser desorption/ionization mass spectrometry (MALDI-MS) of single and intact embryos or oocytes from human, bovine, sheep and fish. The characteristic lipid (represented by GPCho, SM and TAG) profiles were obtained with high mass resolution. However, due to the lateral resolution of the applied methodology (typically >50 µm), limited spatial distribution can be obtained. Time-of-flight secondary ion mass spectrometry (ToF-SIMS) is another major technique for MSI of low-medium mass species, offering much higher spatial resolution. The technique involves scanning the sample surface with a finely-focused energetic (keV) primary ion beam (for example C_{60}^+ or Au_3^+) and recording the ejected secondary ions as a function of their mass to charge ratio (*m/z*) and point of origin on the sample to form a 'chemical map'. The introduction of polyatomic primary ion beams such as C_{60}^+ has facilitated the analysis of molecular species beyond the sample surface allowing complex chemical distributions to be studied in both 2D and 3D (14, 17). Previously, we demonstrated the first ToF-SIMS 3D chemical imaging of a biological cell using the *X. laevis* oocyte as a model system (18). A C_{60}^+ ion beam was used to demonstrate biomolecular depth profiling in the frog oocyte. The spatial distribution of cholesterol (*m/z* 369) and other lipids at *m/z* 540-570 and 800-1000 were revealed to a depth of ~50 µm beneath the oocyte surface.

This study demonstrated proof-of-principle, but practical implementation of high resolution 3D imaging using ToF-SIMS was at that time restricted by existing instrumentation.

We have recently reported on the development and application of a new generation of ToF-SIMS instrumentation, the J105 3D Chemical Imager (Ionoptika Ltd., Southampton, UK), the details of which are described elsewhere (15). The instrument utilizes a DC primary ion beam and buncher-ToF mass analyser. This mode of operation offers high mass resolution without sacrificing lateral resolution, improved duty cycle and independence of mass resolution and mass accuracy from sample topography. These properties are well-suited for studying biological events in topographically challenging samples, including the intact frog embryo. The aim of the current study is to gain new insights into the 2D and 3D arrangement of lipids and other important biomolecules during normal development of *X. laevis* embryos.

Material and methods

Obtaining gametes

X. laevis were bred in the Faculty of Life Science at the University of Manchester. The gametes were obtained and fertilisation was performed using standard procedures (19). The operations were conducted in conformity with the Public Health Service (PHS) Policy on Humane Care and Use of Laboratory Animals, incorporated in the Institute for Laboratory Animal Research (ILAR) Guide for Care and Use of Laboratory Animals. *X. laevis* females were pre-primed subcutaneously 3 to 5 days before use with 50 units of pregnant mare serum gonadotropin (PMSG). 12-18 h before use, the animals were injected subcutaneously with 500 units of human chorionic gonadotrophin (HCG), and placed at 16-18 °C overnight in individual tanks. The next day, animals were transferred to tanks containing 5000 ml 1×Marc's modified Ringer's solution (MMR, in mM: 1000 NaCl, 20 KCl, 10 $MgCl_2$, 20 $CaCl_2$, 50 Hepes = 10×stock solution, pH 7.5, autoclaved before use and diluted accordingly. Except for Hepes purchased from

Biomol, the other chemicals were obtained from Sigma, BioReagent). The laid eggs were then collected in MMR with a wide-bore pipette. Male frogs were sacrificed by lethal injection of 400 µl of 40% ethyl 3-aminobenzoate methanesulfonate (MS-222, Sigma, 98%). The testis were then dissected and stored in L-15 cell culture media (Sigma) at 4 °C for up to 1 week. Fertilisation was then performed by passing a piece of dilacerated testis over the oocytes for 2 min.

Total lipid extraction

A lipid extraction from *X. laevis* zygote was initially analysed to explore the capability of the J105 ToF-SIMS instrument to distinguish the lipid species in a complicated chemical environment and to provide reference spectra for subsequent imaging studies. Methyl tertiary butyl ether (MTBE) extraction of lipids from *X. laevis* zygotes 10 min after fertilization was employed as follows (20). Ten zygotes 10 min post-insemination of the same batch were washed by HPLC water (Sigma-Aldrich) three times and aspirated to remove all the liquid. Subsequently the cells were homogenized in a glass homogenizer and transferred into a glass tube with a Teflon-lined cap, the remaining residue was washed with 1.5 ml methanol (Sigma-Aldrich, CHROMASOLV® Plus, for HPLC, ≥99.9%) and mixed with the homogenized zygotes into the glass tube. 5 ml MTBE (Sigma-Aldrich, CHROMASOLV® Plus, for HPLC, ≥99.9%) was then added into the mixture followed by incubation for 1 h at room temperature on a shaker. Phase separation was induced by adding 1.25 mL MS-grade water. After 10 min of incubation at room temperature, the sample was centrifuged at 1000 g for 10 min. The upper phase was collected, and the lower phase was re-extracted with 2 mL of the solvent mixture ($V_{MTBE/methanol}$=10:3). The total organic phases were divided into 10 aliquots and dried in a vacuum centrifuge for approximately 40 min. To speed up sample drying, 20 µl of MS-grade methanol was added to the organic phase individually after 25 min of centrifugation. The lipid extract was dissolved into 500 µl mixed solvent ($V_{chloroform:methanol:water}$=60:30:4.5) and stored at -20 °C before

analysis. Prior to analysis, 20 µL solution of lipid extract acquired via the above procedure was pipetted onto a silicon wafer and air-dried. Once dried, the samples were transferred immediately into the ToF-SIMS instrument.

Sampling the *X. laevis* embryos

After fertilisation, the eggs were divided into two groups. One group was dejellied 7 min after the start of fertilisation by immersing the eggs in 2% L-cysteine [Sigma, BioUltra, ≥98.5% (RT)] in 0.1×MMR (pH to ~7.5-8.0 with 10 M NaOH) and gently agitated by hand for 2 min. The L-cysteine solution was then decanted and the eggs washed with 0.1×MMR three times within 1 min. The eggs were left in fresh 0.1×MMR. From this time point the fertilized embryos were collected using a pipette every 10 min until 40 min post-fertilisation, and immediately fixed with MEMFA [4% (V/V) formaldehyde solution in mM: 2 EGTA, 1 $MgSO_4$, 20 MOPS, 1.23×10^3 CH_2O. All chemicals are from Sigma, EGTA for molecular biology; $MgSO_4$, BioReagent; Formaldehyde, for molecular biology 36.5-38% in H_2O] for 1.5 h on a shaker and then washed with 1xphosphate buffered saline (PBS) (Sigma, BioReagent, without calcium chloride and magnesium chloride, 10x concentration, diluted accordingly) 4 times and stored in 1x PBS in the fridge (21). Thus, the zygotes 10, 20, 30 and 40 min after the fertilisation were prepared. The other group was dejellied using the same procedure as the first group at 40 min post-insemination, and left in 0.1×MMR at room temperature for further cleavage. The healthy embryos at each cleavage stage were selected, and followed by fixation using MEMFA and washing using 1×PBS as same as the first group to prepare the embryos at 2 cells stage, 4 cells stage, 8 cells stage, 16 cells stage, and furthermore, at different cleavage stages. Since the eggs fertilised *in vitro* at the same time develop almost synchronically (22), the embryos of different cell stages could be collected at certain time intervals, using optical microscopy to confirm the developmental stage.

Prior to ToF-SIMS analysis, the fixed samples were quickly washed with HPLC water three times within 60 s to remove buffer. This was possible without disrupting the integrity of the system due to the resistance of the cell membrane to the osmotic pressure (23, 24). The cells were then loaded onto the SIMS sample holder with the animal hemisphere upwards. After the aspirating the liquid around the cells, the samples were plunge frozen into liquid nitrogen (LN_2), followed by freeze-drying (Heto Drywinner, Thermo Electron Corporation) for 6 h. Under the protection of argon gas, the dried samples were then inserted into the ToF-SIMS instrument.

ToF-SIMS analysis

Mass spectra and images were acquired in positive ion mode with a J105 *3D Chemical Imager* (Ionoptika Ltd, U.K.) using a 40 keV C_{60} primary ion source operating in DC mode. The zygote 10 min post-fertilisation and embryos at different development stages were analysed. In this work the C_{60}^+ beam was operated at a modest 4 µm focus to match the pixel size of data acquisition allowing the entire sample to be imaged in ~45 min. 3D analysis was performed by acquiring sequential image frames with increasing primary ion fluence, thereby revealing the lateral chemical distribution as a function of depth. The mass spectral images were produced using Analyze software (Ionoptika Ltd, UK). Further principal components analysis (PCA) was performed using MATLAB R2009a (The Mathworks Inc. Natick, USA) for better contrast or 3D visualization (analysis routines were developed in-house). The assignment of SIMS ions in the following discussion to lipid classes and specific lipids is consistent with published literature but remains putative at this stage. Further analysis by MS/MS and use of authentic standards would increase confidence in lipid identification.

RESULTS AND DISCUSSION

ToF-SIMS analysis of lipid extracts from zygotes

The ToF-SIMS analysis of extracted lipids from the zygotes was performed to provide reference spectra for the single embryo analysis. The positive ion mass spectrum is shown in Fig. 1. The assignment of major peaks based on published literature using MS is listed in Table 1 (25). The mass accuracy of all listed peaks is better than 10 ppm. All the *m/z* values are rounded to one decimal place in the following description.

The major lipid classes in the lipid extraction could be detected in a single run. The characteristic fragments as well as the molecular ions can be used to assign the lipids. GPCho produces intense fragments at *m/z* 86.1, 104.1, 125.0, 166.1, 184.1 and 224.1 from the phosphocholine headgroup. The glycerol tail of GPCho is mainly fragmented to monoglycerol phosphate at *m/z* 459.3 (C20:3), various monoacylglycerol (MAG) and diacylglycerol (DAG) species and potassiated diacylglycerol phosphate at *m/z* 721.5 (C34:3), 723.5 (C34:2), 725.5 (C34:1). Sphingolipids, including sphingomyelin (SM), share common fragments derived from the phosphocholine headgroup with GPCho. However, instead of two fatty acyl groups bonded to a glycerol back bone, SM has a fatty acyl group bonded to a basic nitrogen leading to the unique ion at *m/z* 265.2 $[C_{18}H_{35}N]^+$, loss of phosphocholine head group and neutral loss of the fatty acid as a ketene. There are some less abundant lipids such as glycerophosphoethanolamine (GPEtn) and glycerophosphoserine (GPSer). GPEtn has characteristic peaks at *m/z* 124.1 and 142.1. Some common fragments are expected due to phospholipids having the same structure of glycerol back bone and phosphate group, e.g., *m/z* 125.0 $[C_2H_6PO_4]^+$ and *m/z* 143.1 $[C_2H_8O_5P]^+$. Schematic fragmentation paths are shown in Fig.2 (25). Several phospholipid species are detected as molecular ions such as 32:1, 34:2, 34:1, 38:4, 38:6 GPCho, 36:2, 36:1, 41:3 GPEtn and sodiated 34:1 SM. The results are consistent with the observations of Hill and co-workers (3). Cholesterol has the characteristic fragments at *m/z* 369.4 $[M+H-H_2O]^+$ and *m/z* 385.4 $[M-H]^+$. The molecular ion of vitamin E ion is observed at *m/z* 430.4. The assignment of various DAG and TAG species in the region

m/z > 500 benefited from the available mass resolution (*m/Δm* 5000). DAG could be the degradation products of TAG and phospholipids as opposed to ion beam induced changes to the structure, however, DAG type lipid fragments do not normally arise from protonated PC containing species as during fragmentation the charge stays on the head group. Fragmentation of the Na and K adducts could also lead to the DAG peaks (34). Considering the abundant DAG and TAG in the frog egg yolk (22), these two lipids are listed individually in Table 1.

ToF-SIMS analysis of a lipid extraction of *X. laevis* zygotes demonstrates that the technique is capable of detecting the major classes of lipid species within complex mixtures without prior chromatographic separation. The characteristic peaks of GPEtn, GPCho, GPSer, GPGro, SM, cholesterol, Vitamin E and DAG are identified and can be used as reference signals to locate the lipid species on the real zygote surface. However, as noted above, without tandem MS verification these assignments could be uncertain due to possible isobaric interferences. Our caution has been demonstrated by listing possible alternative assignments in Table 1. For example, *m/z* 725.5 could be potassiated diacylglycerol phosphate or sodiated SM 34:1.

Monitoring the lipid distribution on the animal hemisphere of zygotes sampled shortly after fertilisation

The fertilisation of eggs is initiated with sperm entry in the 'animal' hemisphere. For *X. laevis*, studies have indicated significantly higher number of spermatozoa binding to the animal hemisphere (35, 36). The first visible sign of egg activation is the movement of pigment granules towards the animal pole (termed cortical contraction), which occurs approximately 4 minutes after fertilisation (37). Our aim was to investigate the biological phenomenon on the surface of the egg shortly after the fertilisation. The zygotes fixed at 10 min post-fertilisation were analysed using a 4 µm-focused 40 keV C_{60}^+ primary ion beam to visualize any local differences of surface chemistry.

Image data acquired from the animal hemisphere of the zygote was binned to 0.1 Da to facilitate data processing. PCA was used to identify the significant differences in the image, and positive loaded peaks in PC2 (Fig. 3) guided the selection of *m/z* values to generate selected ion images as in Fig. 4 (25).

The overall morphology of the zygote is clearly seen in the total ion image shown in Fig. 4 (a). Several features with distinctive chemical gradients are scattered across the zygote surface, the same phenomenon has not been seen in the unfertilised egg surface (data not shown). This indicates that these circular features could be the sperm entry sites. The abundant biomolecules residing within these features are mapped across the animal side of the zygote as in the diagnostic secondary ion images, revealing the varying distribution patterns for different lipids. The common fragment *m/z* 165.1 shared by all glycerophospholipids is spread across the feature areas; *m/z* 166.1 and 184.1 from GPCho and/or SM condense in the middle of the features particularly in one area marked with a white circle in Fig. 4 (d, e); GPGro at *m/z* 189.1 is spread more widely across the features; an unidentified ion at *m/z* 202.1 and GPCho ion at *m/z* 224.1 appear to circle the features in Fig. 4 (g, h), while another SM fragment at *m/z* 265.2 (Fig. 4 (i)) is strongly localised within the distribution of *m/z* 224.1. The other components such as MAG at *m/z* 313.3, cholesterol at *m/z* 369.4 and possible DAG at *m/z* 577.5 are concentrated in the centre of the features as shown in Fig. 4 (j, k, l).

The 3D intensity maps of selected ions are further formed by normalising the intensity of selected ions on each pixel to the maximum intensity of selected ions across the fusion site marked with the white circle in Fig. 4 (a). Peaks at *m/z* 142.1 (Fig. 5(b)) from GPEtn and *m/z* 577.5 (Fig. 5 (f)) from DAG reach higher intensity in the centre of the fusion site, whereas *m/z* 224.1 (Fig. 5 (d)) from GPCho shows more uniform intensity extending to the outer region of the fusion site, *m/z* 265.2 (Fig. 5 (e)) from SM is more tightly distributed at the fusion centre,

as with possible DAG. Combining the information from Fig. 4 and Fig. 5 the pattern of intensity changes across the region of interest, implying different distribution patterns of the selected biomolecules across the feature areas. GPCho is in the outer circle of the fusion site, GPEtn and SM are distributed more towards the fusion centre, and DAG and cholesterol are most abundant in the centre.

Membrane fusion is a profound biological process likely involving lipid rearrangement and possible synthesis. As DAG could be derived from TAG and phospholipids, a similar distribution pattern of DAG at *m/z* 577.5 is expected as phospholipid fragments at *m/z* 166.1 and 224.1, however they show different locations in Fig. 4 (d, h and i). It was also thought that the cleavage of phosphatidylinositol 4,5-bisphosphate (PIP2) into DAG during the fertilisation is involved in the egg activation (38). Therefore, it is likely that DAG ion detected in the fusion site reflects the biological process rather than beam induced fragmentation. Considering that DAG can be rapidly phosphorylated to phosphatidic acid (GPA), which is a critical step in phospholipid biosynthesis (39, 40), it is speculated that in the centre of the fusion site phospholipase-mediated hydrolysis of SM and PIP2 occurs to generate possible DAG (41), which quickly builds new lipids such as GPEtn and GPCho to stop the dissolution of the membrane induced by the sperm binding. GPEtn is able to form highly curved structures that could be used to seal a space inside the fusion centre for the release of the sperm nucleus. Most synthesized GPCho is transported away from the centre to form the outer layer of the fusion site. This proposed model involving lipid synthesis and rearrangement can explain the distribution pattern of selected ions. For example, DAG and SM have high relative intensity exclusively in the fusion centre; GPEtn only exists in the fusion centre and GPCho is lower in the centre and higher away from the centre.

To investigate the fusion progression beneath the surface, depth profiling ToF-SIMS analysis was further performed on the zygote. The distribution of total ion intensity and an image of *m/z* 165.1 are shown for different depth layers (Z1 to Z5) in Fig. 6. This reveals that the fusion sites penetrate the cell membrane and expand with ring-like structures over the depth of the analysis (~100 nm in total, based on the estimated etch rate using the 40 keV C_{60}^+ beam). At this point, it is difficult to identify which fusion site is truly the point of sperm entry. Amphibians contain two groups of mechanisms exhibiting very different blocks to polyspermy (42). One is a fast electrical block before second sperm-egg fusion by cortical granule exocytosis at the fertilization envelope. Another is a slow process that occurs in the egg cytoplasm after sperm entry, allowing only a single sperm nucleus with a single centrosome to ultimately participate in embryonic development, while the other sperm nuclei and centrosomes degenerate before cleavage (43). It is likely that the slow block occurs in the sampled zygote as several fusion sites penetrating the *X. laevis* egg membrane are seen in Fig. 6.

Monitoring the lipid distribution on *Xenopus laevis* embryos through the early development stages

Mitotic cell division, a regulated dynamic biological event, is of such central importance for animal development and associated dynamic processes that the visualization of the mitosis directly in the developing embryo is of great interest. However, only the species featuring a transparent embryo that develops extracorporally (*e.g.* teleosts) can be observed noninvasively by optical microscopy (44). With regard to amphibian embryos with almost complete optical opacity, such as the *X. laevis* embryo, observations are restricted. In this section, ToF-SIMS is employed to monitor the lipid distribution in the ~10 nm surface region through early embryo development offering an alternative, chemically specific, method for embryonic study.

The biomolecular arrangements on the animal hemisphere of embryos at the 2-, 4- and 32-cell stages and blastulas at 3.3 h and 5.5 h post-fertilisation are shown in the positive ion mode ToF-SIMS images in Fig. 7(data previewed from (45)). During the cleavage, the embryo will not grow, but divides into smaller cells called blastomeres packed within the sphere. This morphological change is clearly reflected in the total ion images in Fig. 7(a, a1, a2, a3). The phosphocholine lipid headgroup fragments at *m/z* 125.0, *m/z* 166.1 and *m/z* 184.1 imaged at the 2-cell and 32-cell stages concentrate in the blastomere junctions, and are less intense on the cell surface at these developmental stages as shown in Fig. 7(b, b2, c, c2, d, d2). This species is more uniformly distributed on the embryo at 8-cells stage as in Fig. 7(b1, c1, d1). Cholesterol (*m/z* 369.4) and the possible DAG ion at *m/z* 577.5 spread on the animal side homogenously as seen in Fig. 7(g1, g2, g3, h1, h2, h3) except for the embryo at the 2-cells stage, where they too appear to concentrate at the blastomere junction. It is worth mentioning that the MAG ion at *m/z* 313.3, shown in Fig. 7(f, f1, f2, f3), shares a similar distribution pattern to cholesterol and DAG. The cholesterol lends the membrane rigidity and mobility (46), which could be a reason why the cholesterol is abundant on the animal hemisphere to keep the membrane lipids stable and to adapt to fast biomolecular rearrangement during the cell cleavage. However, considering the vacuum environment of the ToF-SIMS instrument, cholesterol migration to the surface of the membrane (47) cannot be discounted. The distribution of the SM ion at *m/z* 265.2 shows that SM has a high affinity for cholesterol as it co-locates with cholesterol as shown in Fig. 7(e-e3, g-g3). These two biomolecules are able to pack tightly to form micro-domains that are thought to function as signalling platforms in order to regulate the localization and interactions of proteins (48). The blastula 5.5 h post-insemination appears to show a complementary distribution of phosphocholine to SM, cholesterol, MAG and DAG (Fig. 7 d3-h3) although from the image of the whole embryo the detailed distribution is uncertain due to the relatively small feature size. To explore the lipid distribution at this

development stage would require re-analysis of a smaller region exploiting the high resolution capabilities of the C_{60}^+ microprobe for micron-level spatial localisation.

Conclusion and outlook

Single embryo analysis using ToF-SIMS shows the possibility of spatiotemporal chemical mapping of lipids on an embryo surface with high mass resolution and high spatial resolution. The sample preparation is simple without requiring lipid extraction and retains the pristine chemistry on the cell membrane.

The biological process of fertilisation of *X. laevis* egg is visualised by ToF-SIMS imaging to gain the insight into possible mechanism of egg-sperm fusion on the membrane. Lipids profiling in the possible egg-sperm fusion sites shows DAG is located almost exclusively in the centre along with lower intensity of SM, GPEtn is mainly in the fusion centre and GPCho is more intense in surrounding regions of fusion centre. Cholesterol is evenly distributed over a wider range than DAG, possibly to stabilize the newly formed membrane. The results are consistent with the following lipid synthesis pathway. The phospholipase-mediated hydrolysis of SM-generated DAG in the fusion centre swiftly builds new lipids such as GPEtn and GPCho. GPEtn then forms the highly curved structure in order to seal a space inside the fusion centre for the release of the sperm nucleus. Most synthesized GPCho is transported away from the centre to form the outer layer of the fusion site.

For the first time, intact developing embryos have been imaged using ToF-SIMS with relatively simple sample preparation and without considering the embryonic pigment effect as encountered in the optical microscopic approach. Studies such as this may serve as a starting point to further explore the role of lipid distributions in the mechanisms of biological processes in single cells on the micron and submicron scale, which is currently beyond other techniques.

Acknowledgements

This work was funded by a studentship to HT from the Analytical Trust Fund of the Royal Society of Chemistry. The development and use of the J105 ToF-SIMS instrument was funded by the EPSRC under grant EP/G045623. The authors are grateful to Dr. Arno Christian Gutleb and Prof. Nicholas Winograd for the creative discussions, and to Dr Jimmy Moore for assistance with image processing.

References

1. Andreyev, A. Y., E. Fahy, etc. 2010. Subcellular organelle lipidomics in TLR-4-activated macrophages. *J. Lipid Res.* **51**: 2785-2797.

2. Quehenberger, O., A. M. Armando, etc. 2010. Lipidomics reveals a remarkable diversity of lipids in human plasma. *J. Lipid Res.* **51**: 3299-3305.

3. Hill, W. G., N. M. Southern, etc. 2005. Isolation and characterization of the Xenopus oocyte plasma membrane: a new method for studying activity of water and solute transporters. *Am. J. Physiol. Renal Physiol.* **289**: F217-224.

4. Huang, C. H., M. F. Liang, etc. 2003. The fatty acid composition of oophagous tadpoles (Chirixalus eiffingeri) fed conspecific or chicken egg yolk. *Comp. Biochem. Physiol. A Mol. Integr. Physiol.* **135**: 329-336.

5. Koek, M. M., F. Bakels, etc. 2010. Metabolic profiling of ultrasmall sample volumes with GC/MS: from microliter to nanoliter samples. *Anal. Chem.* **82**: 156-162.

6. Touboul, D., A. Brunelle, etc. 2011. Mass spectrometry imaging: Towards a lipid microscope? *Biochimie* **93**: 113-119.

7. Monroy, A., and B. Baccetti. 1975. Morphological changes of the surface of the egg of Xenopus laevis in the course of development. I. Fertilization and early cleavage. *J. Ultrastruct. Res.* **50**: 131-142.

8. Colombo, R., P. Benedusi, etc. 1981. Actin in Xenopus Development: Indirect Immunofluorescence Study of Actin Localization. *Differentiation* **20**: 45-51.

9. Chow, R. L., and R. P. Elinson. 1993. Local alteration of cortical actin in Xenopus eggs by the fertilizing sperm. *Mol. Reprod. Dev.* **35**: 69-75.

10. Ramirez-Zacarias, J. L., F. Castro-Munozledo, etc. 1992. Quantitation of adipose conversion and triglycerides by staining intracytoplasmic lipids with Oil red O. *Histochemistry* **97**: 493-497.

11. Rogers, W. J., J. W. Prichard, etc. 2000. Characterization of signal properties in atherosclerotic plaque components by intravascular MRI. *Arterioscler. Thromb. Vasc. Biol.* **20**: 1824-1830.

12. Wenk, M. R. 2005. The emerging field of lipidomics. *Nat. Rev. Drug Discov.* **4**: 594-610.

13. Nygren, H., B. Hagenhoff, etc. 2007. Bioimaging TOF-SIMS: High resolution 3D Imaging of single cells. *Microsc. Res. Tech.* **70**: 969-974.

14. Fletcher, J. S., N. P. Lockyer, etc. 2010. Developments in molecular SIMS depth profiling and 3D imaging of biological systems using polyatomic primary ions. *Mass Spectrom. Rev.* **30**: 142-174.

15. Fletcher, J. S., S. Rabbani, etc. 2008. A new dynamic in mass spectral imaging of single biological cells. *Anal. Chem.* **80**: 9058-9064.

16. Ferreira, C. R., S. A. Saraiva, etc. 2011. Single embryo and oocyte lipid fingerprinting by mass spectrometry. *J. Lipid Res.* **51**: 1218-1227.

17. Fletcher, J. S., N. P. Lockyer, etc. 2006. C60, Buckminsterfullerene: its impact on biological ToF-SIMS analysis. *Surf. Interface Anal.* **38**: 1393-1400.

18. Fletcher, J. S., N. P. Lockyer, etc. 2007. TOF-SIMS 3D biomolecular imaging of Xenopus laevis oocytes using buckminsterfullerene (C60) primary ions. *Anal. Chem.* **79**: 2199-2206.

19. Strauss, B., R. J. Adams, etc. 2006. A default mechanism of spindle orientation based on cell shape is sufficient to generate cell fate diversity in polarised Xenopus blastomeres. *Development* **133**: 3883-3893.

20. Matyash, V., G. Liebisch, etc. 2008. Lipid extraction by methyl-tert-butyl ether for high-throughput lipidomics. *J. Lipid Res.* **49**: 1137-1146.

21. Dykstra, M. J., and L. E. Reuss. 2003. Biological electron microscopy: theory, techniques, and Troubleshooting. 2nd ed. Springer. 12-15.

22. Gilbert, S. F. 2010. Developmental Biology. 9th ed. Singuer Association. 96-111.

23. Berntsson, K.-E., B. Haglund, etc. 1965. Osmoregulation in the amphibian egg the influence of calcium. *J. Cell. Comp. Physiol.* **65**: 101-112.

24. Kelly, S. M., J. P. Butler, etc. 1995. Control of cell volume in oocytes and eggs from Xenopus laevis. *Comparative Biochemistry and Physiology Part A: Physiology* **111**: 681-691.

25. Tian, H. 2011. Visualisation and Profiling of Lipids in Single Biological Cells Using Time-of-Flight Secondary Ion Mass Spectrometry. Ph.D Thesis. University of Manchester, Manchester, UK.

26. Ostrowski, S. G., C. Szakal, etc. 2005. Secondary ion MS imaging of lipids in picoliter vials with a buckminsterfullerene ion source. *Anal. Chem.* **77**: 6190-6196.

27. Yang, H.-J., I. Ishizaki, etc. 2010. Detection of characteristic distributions of phospholipid head groups and fatty acids on neurite surface by time-of-flight secondary ion mass spectrometry. *Med Mol Morphol* **43**: 158-164.

28. Tahallah, N., A. Brunelle, etc. 2008. Lipid mapping in human dystrophic muscle by cluster-time-of-flight secondary ion mass spectrometry imaging. *J. Lipid Res.* **49**: 438-454.

29. Pulfer, M., and R. C. Murphy. 2003. Electrospray mass spectrometry of phospholipids. *Mass Spectrom. Rev.* **22**: 332-364.

30. Löhmann, C., E. Schachmann, etc. 2010. Developmental profiling by mass spectrometry of phosphocholine containing phospholipids in the rat nervous system reveals temporo-spatial gradients. *J. Neurochem.* **114**: 1119-1134.

31. Passarelli, M. K., and N. Winograd. 2011. Lipid imaging with time-of-flight secondary ion mass spectrometry (ToF-SIMS). *Biochim. Biophys. Acta* **1811**: 976-990.

32. Kalo, P. J., V. Ollilainen, etc. 2006. Identification of molecular species of simple lipids by normal phase liquid chromatography–positive electrospray tandem mass spectrometry, and application of developed methods in comprehensive analysis of low erucic acid rapeseed oil lipids. *Int. J. Mass Spectrom.* **254**: 106-121.

33. LIPID MAPS Lipid Structure Database (LMSD). http://www.lipidmaps.org/data/structure/LMSDSearch.php?Mode=ProcessClassSearch&LMID=LMGL03 (Accessed April 10th 2014).

34. Passarelli, M. K., and N. Winograd. 2011. Characterizing in situ Glycerophospholipids with SIMS and MALDI Methodologies. *Surf. Interface Anal.* **43**: 269-271.

35. Stein, K. K., P. Primakoff, etc. 2004. Sperm-egg fusion: events at the plasma membrane. *J. Cell Sci.* **117**: 6269-6274.

36. Katagiri, C., N. Yoshizaki, etc. 1999. Analyses of oviductal pars recta-induced fertilizability of coelomic eggs in Xenopus laevis. *Dev. Biol.* **210**: 269-276.

37. Stewart-Savage, J., and R. D. Grey. 1982. The temporal and spatial relationships between cortical contraction, sperm trail formation, and pronuclear migration in fertilized Xenopus eggs. *Dev. Genes Evol.* **191**: 241-245.

38. Larabell, C., and R. Nuccitelli. 1992. Inositol lipid hydrolysis contributes to the Ca2+ wave in the activating egg of Xenopus laevis. *Dev. Biol.* **153**: 347-355.

39. Luo, B., D. S. Regier, etc. 2004. Diacylglycerol kinases. *Cell. Signal.* **16**: 983-989.

40. Athenstaedt, K., and G. Daum. 1999. Phosphatidic acid, a key intermediate in lipid metabolism. *Eur. J. Biochem.* **266**: 1-16.

41. Berridge, M. J. 1993. Inositol Trisphosphate and Calcium Signaling. *Nature* **361**: 315-325.

42. Tarin, J. J., and A. Cano. 2000. Fertilization in protozoa and metazoan animals: cellular and molecular aspects. illustrated ed. Springer.

43. Glahn, D., and R. Nuccitelli. 2003. Voltage-clamp study of the activation currents and fast block to polyspermy in the egg of Xenopus laevis. *Dev. Growth Differ.* **45**: 187-197.

44. Papan, C., B. Boulat, etc. 2006. Time-lapse tracing of mitotic cell divisions in the early Xenopus embryo using microscopic MRI. *Dev. Dyn.* **235**: 3059-3062.

45. Large Complex Samples. http://www.ionoptika.com/j105-features/119-applications/j105-features/144-large-complex-samples.html (Accessed April 10th 2014).

46. van Meer, G., D. R. Voelker, etc. 2008. Membrane lipids: where they are and how they behave. *Nature Reviews. Molecular Cell Biology* **9**: 112-124.

47. Jones, E. A., N. P. Lockyer, etc. 2008. Depth Profiling Brain Tissue Sections with a 40 keV C60+ Primary Ion Beam. *Anal. Chem.* **80**: 2125-2132.

48. Milhas, D., C. J. Clarke, etc. 2010. Sphingomyelin metabolism at the plasma membrane: Implications for bioactive sphingolipids. *FEBS Lett.* **584**: 1887-1894.

Fig. 1. Positive ion mode ToF-SIMS spectrum of a lipid extraction from *Xenopus laevis* zygote 10 min after fertilisation. Spectral dose density was 1×10^{13} ions/cm^2 using a 40 keV C_{60}^+ beam. Data acquired with mass resolution $m/\Delta m$ ~5000

Fig. 2. Fragmentation of the major classes of lipids in biological cell membranes. Adapted from (25).

Fig. 3. PCA loadings plot of ToF-SIMS data of single *Xenopus laevis* zygote 10 min post-insemination. Inset is PC2 scores image which shows that positive loadings (shown in green) contribute to the possible fusion site of the gametes on the animal hemisphere of the zygote. ToF-SIMS signals associated with the possible fusion site on the animal pole of the zygote are labelled in the positive loading in PC2. Adapted from (25).

Fig. 4. Total ion and selected ion images (positive mode ToF-SIMS) of the animal hemisphere of *Xenopus laevis* zygote 10 min post-insemination. Spectral dose density is 5×10^{13} ions/cm^2 using a 4 µm-focused 40 keV C_{60}^+ beam over 1200×1200 µm^2 with 256×256 pixels. The surface region marked with a white circle is the proposed egg-sperm fusion site. *m/z* 165.1 is a common glycerophospholipid fragment; *m/z* 166.1 and 184.1, the fragments from GPCho and SM; *m/z* 224.1, the fragment from GPCho; *m/z* 265.2, the characteristic peak of SM; *m/z* 313.3, MAG $[C_{19}H_{37}O_3]^+$ C16:0; *m/z* 369.4, cholesterol fragment; *m/z* 577.5, DAG $[C_{37}H_{69}O_4]^+$ C34:1; *m/z* 152.1, 189.1 and 202.1 are unassigned ions. The colour scale corresponds to the relative ion intensity and the maximum count (mc) per pixel is displayed in each image frame. Adapted from (25).

Fig. 5. 3D intensity map of total ions and selected ions across the proposed fusion site identified in Fig 4(a). Selected peak assignment is as follows, *m/z* 142.1 fragment from GPEtn; *m/z* 166.1,

fragment from GPCho and SM; *m/z* 224.1,fragment of GPCho; *m/z* 265.2, fragment of SM; *m/z* 577.5, DAG $[C_{37}H_{69}O_4]^+$ C34:1.

Fig. 6. Depth profile of *Xenopus laevis* zygote 10 min post-insemination using dynamic ToF-SIMS imaging (positive mode ToF-SIMS) with a 4 µm-focused 40 keV C_{60}^+ beam, showing that the gametes fusion progressed through the surface region. The distribution of total ion signal (top row) and *m/z* 165.1 (bottom row) is shown as a function of depth (Z1 to Z5, ~20 to 100 nm total depth). The depth profiling was performed on the animal hemisphere. Starting from the image at the surface (Z1) each image was acquired with an additional primary ion dose density of 1×10^{13} ions/cm^2 over an area of 1200×1200 µm^2 (256×256 pixels).

Fig. 7. Total ion and selected ion images (positive mode ToF-SIMS) of the animal hemisphere of *Xenopus laevis* embryos in different cleavage stages using dynamic ToF-SIMS imaging. The 40 keV C_{60}^+ beam primary ion dose density was 2×10^{13} ions/cm^2 over a 1200×1200 µm^2 area with 256 × 256 pixels. The biomolecular arrangements on the animal hemisphere of embryos at 2 cells, 4 cells, 32 cells and blastula 5.5 h post-insemination are shown. During the cleavage the embryo will not grow but divide into smaller cells (blastomeres) packed on the surface of the sphere. The maximum counts (mc) can be read on the ion images. *m/z* 165.1, common fragment from glycerophospholipids; GPCho and SM share the fragments at *m/z* 125.0, 166.1, 184.1, *m/z* 265.2 is unique to SM; *m/z* 313.3, MAG $[C_{19}H_{37}O_3]^+$ C16:0; *m/z* 369.4, cholesterol fragment; *m/z* 577.5, DAG $[C_{37}H_{69}O_4]^+$ C34:1 or the fragment from phospholipid. (Data previewed from (45)).

Table 1. Characteristic molecular ions and fragments of common lipids in ToF-SIMS spectra. Adapted from (25).

	+SIMS			
	m/z	**Proposed fragments**	**Species**	**Reference**
Glycerophospho-choline (GPCho)	86.1188	$[C_5H_{12}N]^+$	Fragment	(18, 26)
	104.1198	$[C_5H_{14}NO]^+$	Fragment	(27)
	125.0016	$[C_2H_6PO_4]^+$	Fragment	(28)
	166.0716	$[C_5H_{13}NPO_3]^+$	Fragment	(18, 26)
	184.0717	$[C_5H_{15}NPO_4]^+$	Fragment	(18, 26)
	206.0717	$[C_5H_{14}NPO_4Na]^+$	Fragment	(18, 26)
	224.1192	$[C_8H_{19}NPO_4]^+$	Fragment	(28)
	246.0978	$[C_8H_{18}NPO_4Na]^+$	Fragment	(27)
	459.2727	$[C_{23}H_{40}O_7P]^+$ C20:3 monoglycerolphosphate	Fragment	(29)
	478.3416	$[C_9H_{18}NPO_6\text{-}C_{15}H_{31}]^+$ C16:0 monoacylglycero-phosphocholines	Fragment	(29, 30)
	496.3012	$[C_9H_{20}NPO_7\text{-}C_{15}H_{31}]^+$ C16:0 monoacylglycero-phosphocholines	Fragment	(29, 30)
	521.4268	$[C_{33}H_{61}O_4]^+$ C30:1	Fragment	(29)
	523.4391	$[C_{33}H_{63}O_4]^+$ C30:0	Fragment	(29)
	721.4575	$[C_{39}H_{71}O_7PK]^+$ C34:3	$[M+K\text{-}TMA]^+$	(31)
	723.4828	$[C_{39}H_{73}O_7PK]^+$ 34:2	$[M+K\text{-}TMA]^+$	(31)
	725.5492	$[C_{39}H_{75}O_7PK]^+$ C34:1	$[M+K\text{-}TMA]^+$	(28, 31)
	732.5794	$[C_{10}H_{19}NPO_8\text{-}C_{30}H_{60}]^+$ C32:1	$[M+H]^+$	(3)
	758.5543	$[C_{10}H_{19}NPO_8\text{-}C_{32}H_{62}]^+$ C34:2	$[M+H]^+$	(3)
	760.5859	$[C_{10}H_{19}NPO_8\text{-}C_{32}H_{64}]^+$ C34:1	$[M+H]^+$	(3)
	780.5659	$[C_{42}H_{80}NPO_8Na]^+$ C34:2	$[M+Na]^+$	(28)
	782.5727	$[C_{42}H_{82}NPO_8Na]^+$ C34:1	$[M+Na]^+$	(28)
	784.5800	$[C_{42}H_{84}NPO_8Na]^+$ C34:0	$[M+Na]^+$	(28)
	798.5834	$[C_{42}H_{82}NPO_8K]^+$ C34:1	$[M+K]^+$	(28)
	806.5659	$[C_{10}H_{19}NPO_8\text{-}C_{36}H_{62}]^+$ C38:6	$[M+H]^+$	(3)
Glycerophospho-ethanolamine (GPEtn)	124.0946	$[C_2H_7NPO_3]^+$	Fragment	(18, 26)
	142.0712	$[C_2H_9NPO_4]^+$	Fragment	(18, 26)
	743.5283	$[C_7H_{12}NPO_8\text{-}C_{34}H_{66}]^+$ C36:2	$[M+H]^+$	(3)
	745.4645	$[C_7H_{12}NPO_8\text{-}C_{34}H_{68}]^+$ C36:1	$[M+H]^+$	(3)
	811.7188	$[C_7H_{12}NPO_8\text{-}C_{39}H_{74}]^+$ C41:3	$[M+H]^+$	(3)
Glycerophospho-glycerol(GPGro)	198.1008	$[C_5H_{11}PO_6]^+$	Fragment	
	747.4999	$[C_8H_{12}PO_{10}\text{-}C_{32}H_{64}]^+$ C34:1	$[M+H]^+$	(3)
Glycerophospho-	185.0894	$[C_3H_8NPO_6]^+$	Fragment	(18, 26)

serine(GPSer)				
Sphingolipids	86.1188	$[C_5H_{12}N]^+$	Fragment	(18, 26)
	102.0651	$[C_5H_{12}NO]^+$	Fragment	(27)
	104.1198	$[C_5H_{14}NO]^+$	Fragment	(27)
	166.0716	$[C_5H_{13}NPO_3]^+$	Fragment	(18, 26)
	184.0717	$[C_5H_{15}NPO_4]^+$	Fragment	(18, 26)
	206.0717	$[C_5H_{14}NPO_4Na]^+$	Fragment	(18, 26)
	265.2644	$[C_{18}H_{35}N]^+$	Fragment	(29)
	725.5492	$[C_{39}H_{80}N_2PO_6Na]^+$ C34:1	$[M+Na]^+$	(28, 31)
Sterol lipids	369.3567	$[C_{27}H_{45}]^+$	$[M+H-H_2O]^+$	(18)
Cholesterol	385.3290	$[C_{27}H_{45}O]^+$	$[M-H]^+$	(18)
Prenol lipids Vitamin E	430.3663	$[C_{29}H_{50}O_2]^+$	$[M]^+$	(31)
Monoacyl-glycerol (MAG)	311.2531	$[C_{19}H_{35}O_3]^+$ C16:1	All the ions listed here could be fragments from phospholipids, DAG and TAG, or could be $[M+H-OH]^+$ from MAG.	(31)
	313.2756	$[C_{19}H_{37}O_3]^+$ C16:0		(31)
	323.2612	$[C_{20}H_{35}O_3]^+$ C17:2		(32)
	325.2748	$[C_{20}H_{37}O_3]^+$ C17:1		(32)
	327.2948	$[C_{20}H_{39}O_3]^+$ C17:0		(32)
	335.2450	$[C_{21}H_{35}O_3]^+$ C18:3		(32)
	337.2773	$[C_{21}H_{37}O_3]^+$ C18:2		(31)
	339.2876	$[C_{21}H_{39}O_3]^+$ C18:1		(31)
	341.2904	$[C_{21}H_{41}O_3]^+$ C18:0		(31)
	351.2905	$[C_{22}H_{39}O_3]^+$ C19:2		(32)
	353.3179	$[C_{22}H_{41}O_3]^+$ C19:1		(32)
	355.3002	$[C_{22}H_{43}O_3]^+$ C19:0		(32)
	391.2893	$[C_{25}H_{43}O_3]^+$ C22:2		(32)
	393.2867	$[C_{25}H_{45}O_3]^+$ C22:1		(32)
	395.3213	$[C_{25}H_{47}O_3]^+$ C22:0		(32)
Diacylglycerol (DAG)	515.4220	$[C_{33}H_{55}O_4]^+$ C30:0	All the ions listed here could be fragments from phospholipids and TAG, or could be $[M+H-OH]^+$ from DAG.	(31)
	519.4109	$[C_{33}H_{59}O_4]^+$ C30:2		(31)
	545.4204	$[C_{35}H_{61}O_4]^+$ C32:3		(31)
	547.4403	$[C_{35}H_{63}O_4]^+$ C32:2		(31)
	549.4657	$[C_{35}H_{65}O_4]^+$ C32:1		(31)
	551.4621	$[C_{35}H_{67}O_4]^+$ C32:0		(31)
	561.4643	$[C_{36}H_{65}O_4]^+$ C33:2		(31)
	563.4710	$[C_{36}H_{67}O_4]^+$ C33:1		(31)
	571.4325	$[C_{37}H_{63}O_4]^+$ C34:4		(31)
	573.4450	$[C_{37}H_{65}O_4]^+$ C34:3		(31)

	575.4638	$[C_{37}H_{67}O_4]^+$ C34:2		(31)
	577.4696	$[C_{37}H_{69}O_4]^+$ C34:1		(31)
	579.4866	$[C_{37}H_{71}O_4]^+$ C34:0		(31)
	587.4610	$[C_{38}H_{67}O_4]^+$ C35:3		(31)
	589.4792	$[C_{38}H_{69}O_4]^+$ C35:2		(31)
	591.4900	$[C_{38}H_{71}O_4]^+$ C35:1		(31)
	595.4408	$[C_{39}H_{63}O_4]^+$ C36:6		(31)
	597.4587	$[C_{39}H_{65}O_4]^+$ C36:5		(31)
	599.4799	$[C_{39}H_{67}O_4]^+$ C36:4		(31)
	601.4857	$[C_{39}H_{69}O_4]^+$ C36:3		(31)
	603.5008	$[C_{39}H_{71}O_4]^+$ C36:2		(31)
	605.5080	$[C_{39}H_{73}O_4]^+$ C36:1		(31)
	607.3814	$[C_{39}H_{75}O_4]^+$ C36:0		(31)
	621.4608	$[C_{41}H_{65}O_4]^+$ C38:7		(31)
	623.4754	$[C_{41}H_{67}O_4]^+$ C38:6		(31)
	625.4749	$[C_{41}H_{69}O_4]^+$ C38:5		(31)
Triacylglycerol (TAG)	825.6895	$[C_{53}H_{93}O_6]^+$ C50:5	All the ions listed here are $[M+H]^+$ or $[M+Na]^+$.	(31)
	827.6923	$[C_{53}H_{95}O_6]^+$ C50:4		(31)
	829.6723	$[C_{53}H_{97}O_6]^+$ C50:3		(31)
	837.7000	$[C_{54}H_{93}O_6]^+$ C51:6		(31)
	839.7016	$[C_{54}H_{95}O_6]^+$ C51:5		(31)
	849.7359	$[C_{54}H_{97}O_6]^+$ C51:4		(31)
	851.7067	$[C_{55}H_{95}O_6]^+$ C52:6		(31)
	853.7187	$[C_{55}H_{97}O_6]^+$ C52:5/$[C_{53}H_{98}O_6\ Na]^+$ C50:2		(31)
	855.7371	$[C_{55}H_{99}O_6]^+$ C52:4/$[C_{53}H_{100}O_6Na]^+$ C50:1		(31)
	861.6857	$[C_{55}H_{105}O_6]^+$ C52:0		(31)
	863.7032	$[C_{56}H_{95}O_6]^+$ C53:7		(31)
	865.7167	$[C_{56}H_{97}O_6]^+$ C53:6		(31)
	867.7572	$[C_{56}H_{99}O_6]^+$ C53:5		(31)
	877.7266	$[C_{55}H_{98}O_6Na]^+$ C52:4/$[C_{57}H_{97}O_6]^+$ C54:2		(31)
	879.7386	$[C_{55}H_{100}O_6Na]^+$ C52:3/$[C_{57}H_{99}O_6]^+$ C54:3		(31)
	881.7404	$[C_{55}H_{102}O_6Na]^+$ C52:2/$[C_{57}H_{101}O_6]^+$C54:4		(31)
	899.6900	$[C_{59}H_{95}O_6]^+$ C56:10		*(33)
	901.7332	$[C_{59}H_{97}O_6]^+$ C56:9		*(33)
	903.7392	$[C_{59}H_{99}O_6]^+$ C56:8		*(33)
	905.7576	$[C_{59}H_{101}O_6]^+$ C56:7		*(33)
	925.7477	$[C_{59}H_{99}O_6Na]^+$ C56:8		*(33)
	927.7972	$[C_{59}H_{101}O_6Na]^+$ C56:7		*(33)
	929.7967	$[C_{59}H_{103}O_6Na]^+$ C56:6		*(33)

951.7453	$[C_{61}H_{100}O_6Na]^+$ C58:4	*(33)
953.7298	$[C_{61}H_{102}O_6Na]^+$ C58:4	*(33)

Note: * represents the species assigned according to the LIPID MAPS structure database.

Fig. 1

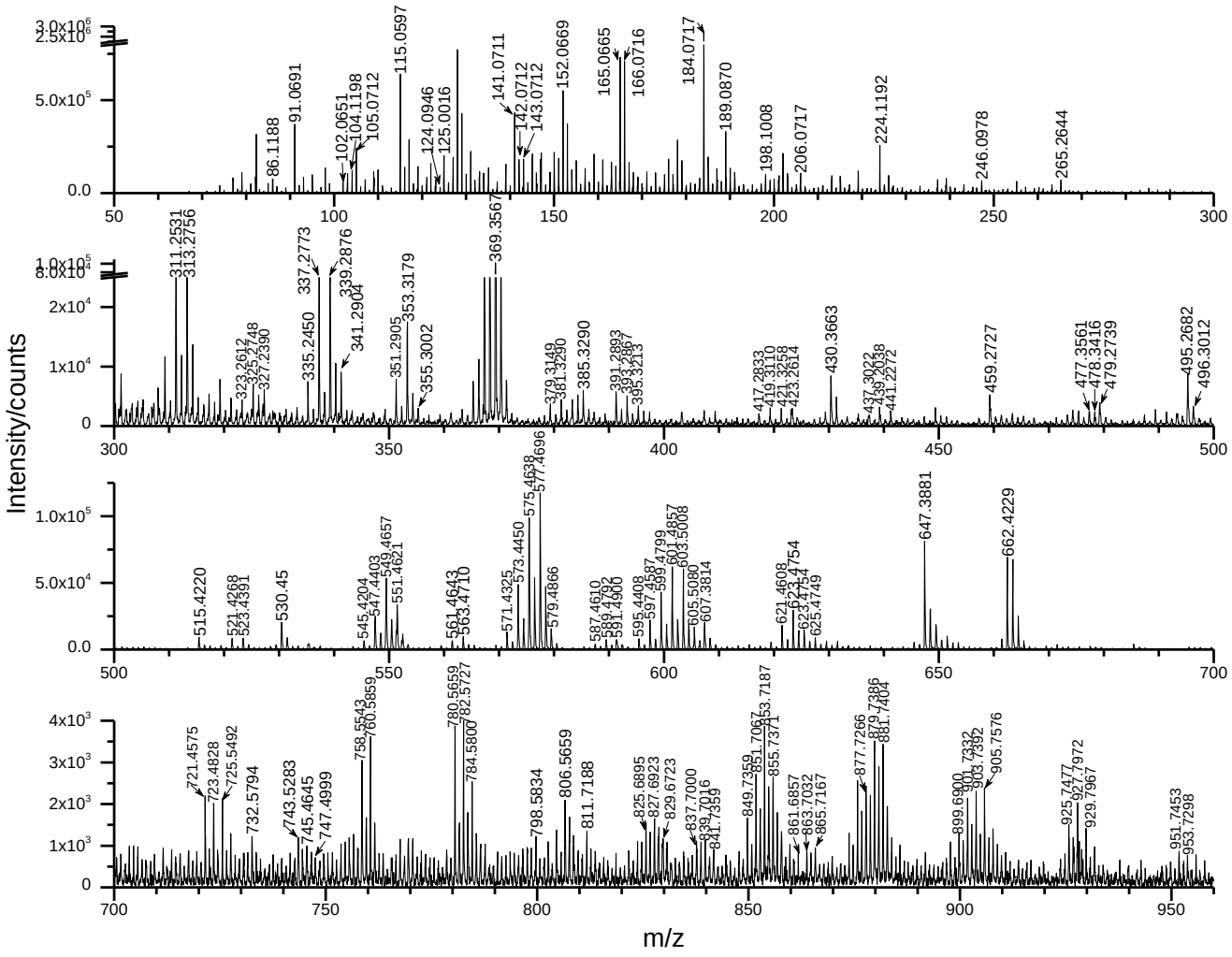

Fig. 2

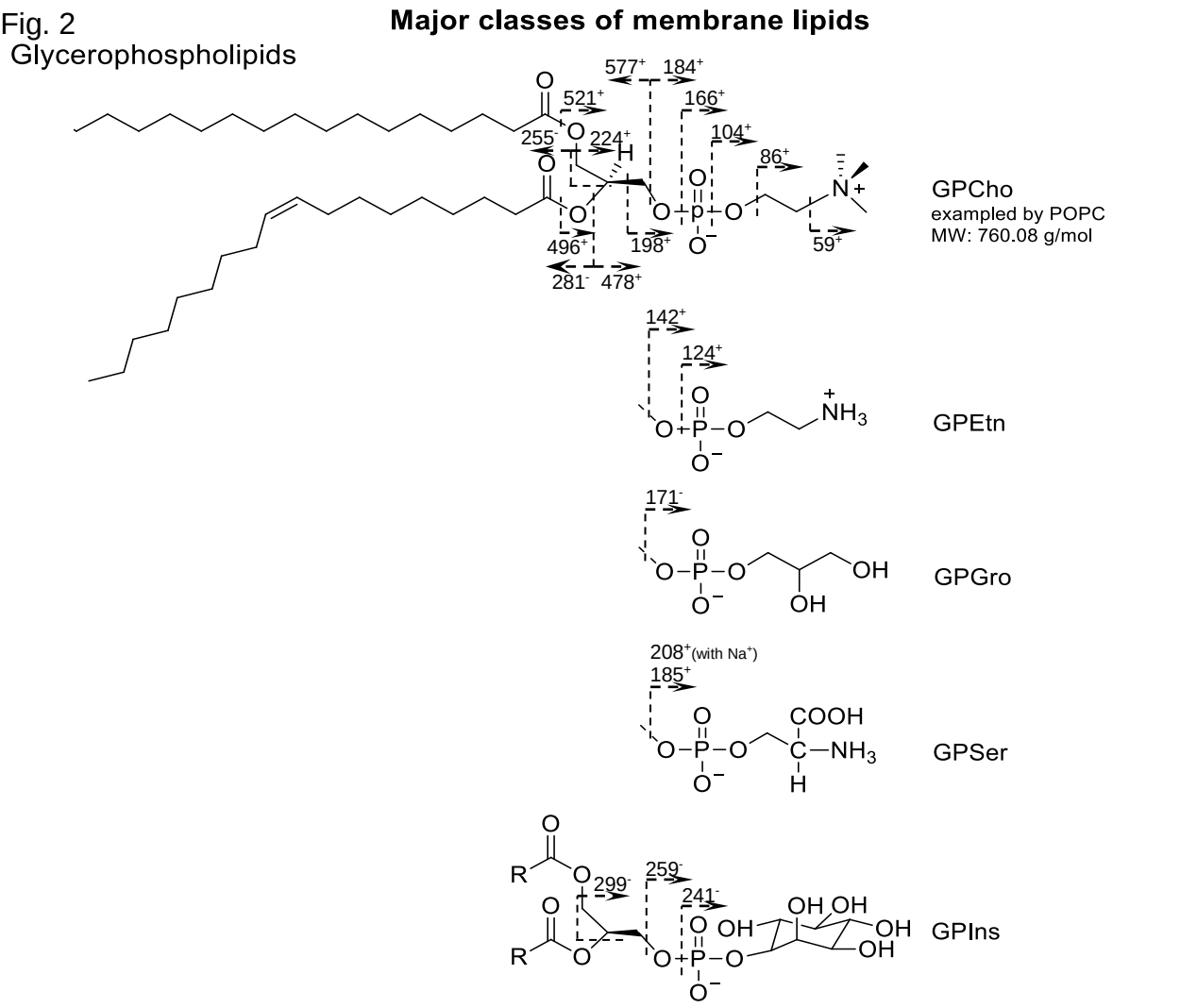

Fig. 3

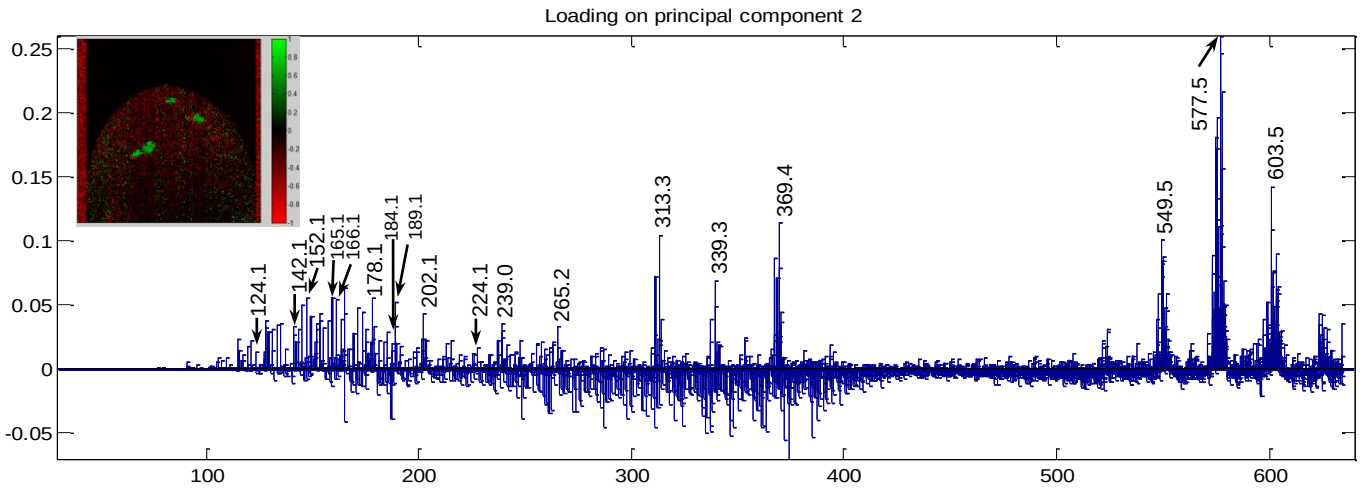

Fig. 4

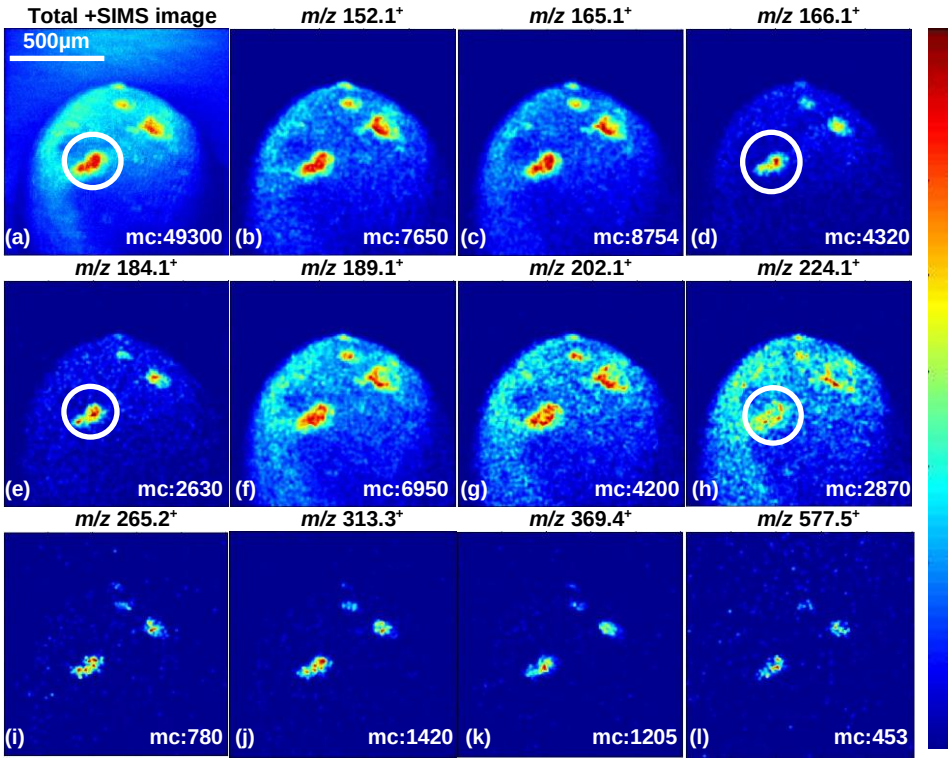

Fig. 5

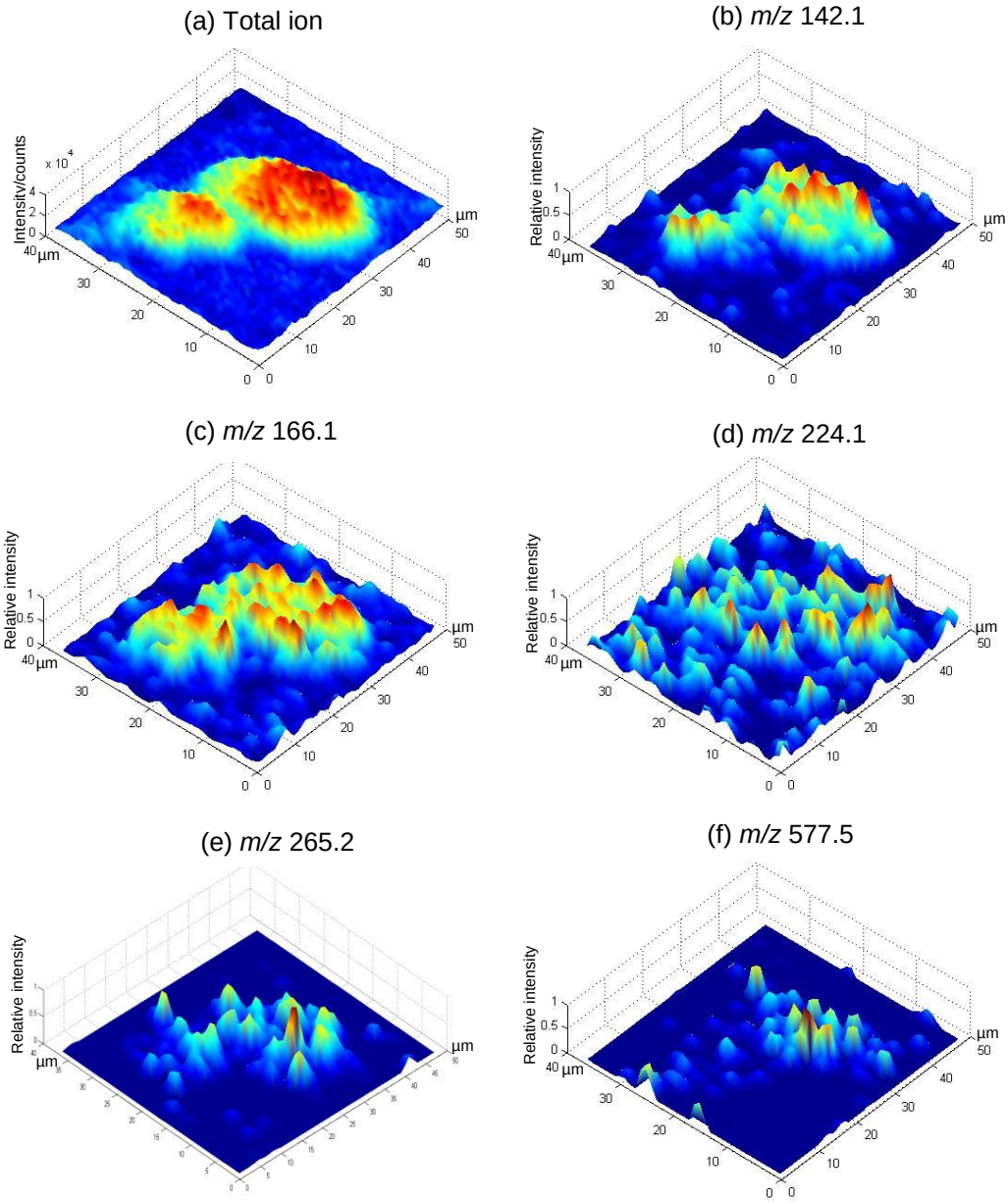

Fig. 6

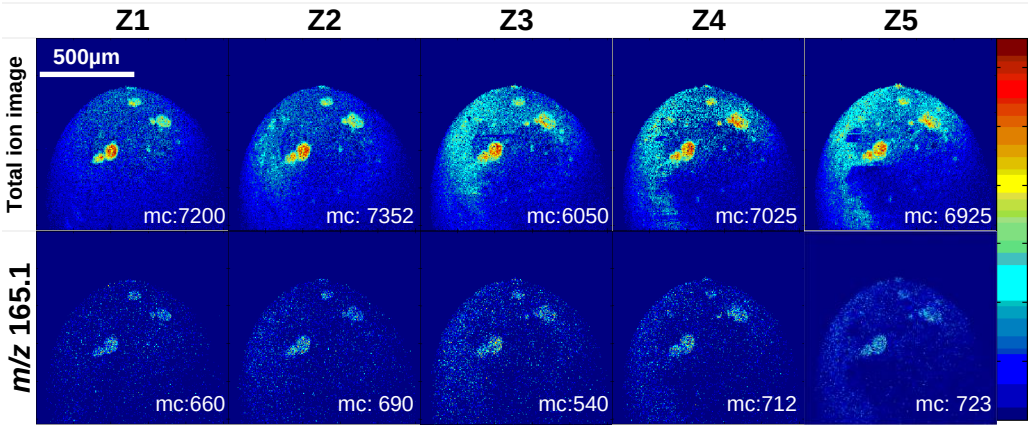

Fig. 7